nature energy

Supplementary information

https://doi.org/10.1038/s41560-026-02120-8

Lithium–disulfur dichloride batteries

In the format provided by the authors and unedited

Supplementary Notes

Supplementary Note 1: Energy-density calculation for binary conversion electrodes

To evaluate the theoretical energy density of binary conversion electrodes, compounds with the general formula AB_m were screened. In most cases, elements A and B differ in electronegativity, in which A represents the more electropositive component and B the more electronegative component. In some cases, A and B can be identical, as elemental materials (for example sulfur and chlorine) were also included in the screening. For element B, non-metal elements with electronegativity values greater than 2 (excluding carbon) were considered. For element A, in addition to the overlapping non-metal elements, several representative transition metals, including Mn, Fe, Co, and Cu, were included.

The Gibbs free energy change (ΔG) of the following conversion reaction was evaluated:

$$AB_m + (a + mb)Li \rightleftharpoons Li_aA + mLi_bB$$

For metallic elements used as component A, the coefficient a was generally set to zero because these metals rarely form stable lithiated compounds. For non-metal elements, a typically ranged from 1 to 3 depending on their lithiation chemistry. The Gibbs free energies of formation of AB_m, Li_aA, and Li_bB were primarily obtained from the NIST Chemistry WebBook.[1] For compounds not available in the NIST database, data from the Materials Project database were used.[2] Because the Materials Project database mainly provides calculated formation enthalpies rather than full Gibbs free energies, the resulting theoretical voltages may deviate slightly from experimental values, typically within ~0.2–0.3 V for solid and liquid compounds.

For certain element combinations in which no experimentally reported stable compounds were available, the Gibbs free energy of formation was approximated as zero to preserve the completeness of the screening dataset, and a 1:1 stoichiometry between A and B was assumed. The theoretical specific capacities were calculated using the total masses of both reactants (AB_m and Li) or products (Li_aA and Li_bB), such that the reported values correspond to the electrode level. The complete dataset ranked by calculated energy density is summarized in **Supplementary Table 1**.

Supplementary Note 2: Optimization of the LiTFSI–EMIMCl–TTE electrolyte

Although the LiTFSI–EMIMCl–TTE electrolyte (LiTFSI, lithium bis(trifluoromethanesulfonyl)imide; EMIMCl, 1-ethyl-3-methylimidazolium chloride; TTE, 1,1,2,2-tetrafluoroethyl 2,2,3,3-tetrafluoropropyl ether) exhibits good reversibility for Li||S–LiCl cells, its cycling stability remains limited. The instability is mainly associated with poor cycling stability of the lithium metal anode. As shown in **Supplementary Figure 29b**, Li symmetric cells using the LiTFSI–EMIMCl–TTE electrolyte remain stable for only ~10 cycles at a current density of 0.2 mA cm^{-2} and an areal capacity of 0.4 mAh cm^{-2}. After ~20 cycles, the overpotential increases substantially and the cell eventually short circuits.

Both lithium bis(fluorosulfonyl)imide (LiFSI) and lithium nitrate ($LiNO_3$) are widely used additives for improving the cycling stability of lithium metal.[3,4] After partially replacing 60% of LiTFSI with 40% LiFSI and 20% $LiNO_3$, the lithium cycling stability improved significantly. This modified electrolyte is denoted as LiTFSI–EMIMCl–TTE–A. As shown in **Supplementary Figure 29a**, Li symmetric cells using LiTFSI–EMIMCl–TTE–A exhibit much improved cycling stability, maintaining stable operation for more than 100 cycles under the same testing conditions.

To further investigate the interfacial chemistry, X-ray photoelectron spectroscopy (XPS) analyses were conducted on cycled lithium metal anodes (**Supplementary Figure 30**). The lithium surface cycled in LiTFSI–EMIMCl–TTE exhibited stronger C–O, C=O, and –CO_3^-/CF_x signals in the C 1s spectra, indicating a larger fraction of organic species in the solid electrolyte interphase (SEI). In contrast, lithium cycled in LiTFSI–EMIMCl–TTE–A showed a much stronger LiF signal, indicating the formation of a LiF-rich SEI. Such an interphase provides improved chemical stability and effectively suppresses lithium corrosion during cycling. The improved lithium reversibility in the modified electrolyte is therefore attributed to the formation of this robust LiF-rich interphase.

Supplementary Note 3: Evaluation of energy contribution from the electrolyte

The presence of Cl^- in the electrolyte may raise concerns regarding its possible contribution to the overall energy density of the cell and the practical evaluation of Li||S–LiCl cells. To address this issue, two key points must be clarified: (1) the operation of the

Li||S_2Cl_2 chemistry does not rely on energy stored in the electrolyte itself, and (2) the contribution of the LiTFSI–EMIMCl–TTE electrolyte to the total cell energy is minimal.

As discussed in the main text, the introduction of EMIMCl into the electrolyte is intended to introduce excess Cl^- relative to the available Li^+ coordination sites and thereby increase the fraction of free Cl^- species. These free Cl^- ions facilitate sulfur oxidation and improve reaction kinetics. Importantly, sulfur oxidation can still occur even in the absence of Cl^- in the electrolyte, provided that LiCl is incorporated within the electrode. To verify this, triethylene glycol dimethyl ether (G3) was selected as the solvent because of its strong coordination with Li^+, which is expected to weaken Li^+–Cl^- interactions. As shown in **Supplementary Figure 35a**, Li||S–LiCl cells using a G3-based electrolyte (2 M lithium difluoro(oxalato)borate (LiDFOB) + 1 M $LiNO_3$) exhibit sulfur oxidation at ~3.7–3.8 V, approximately 0.3 V above the theoretical sulfur oxidation voltage but still below the oxidation potential of pure LiCl (~3.9–4.0 V). A small cathodic peak near ~3.2–3.3 V is observed in the magnified dQ/dV profile (inset of **Supplementary Figure 35b**), indicating that only a small fraction of S_2Cl_2 remains within the electrode because most S_2Cl_2 dissolves into the electrolyte and undergoes severe shuttle behavior, leading to rapid capacity decay. Sulfur oxidation therefore primarily originates from the S–LiCl electrode rather than from electrochemical energy stored in the electrolyte. At the same time, the strong Li^+–Cl^- interactions in the G3 electrolyte further highlight the importance of generating free Cl^- species to facilitate reversible sulfur oxidation.

To further evaluate the possible energy contribution from the electrolyte, Li||S–C cells with areal capacities of ~0.6–0.7 mAh cm^{-2} were tested using either pristine LiTFSI–EMIMCl–TTE electrolyte or LiTFSI–EMIMCl–TTE electrolyte saturated with LiCl. As shown in **Supplementary Figure 36**, the conventional S^{2-}/S^0 redox reaction proceeds normally in both electrolytes, whereas the high-voltage sulfur oxidation process contributes only ~30 mAh g_S^{-1} in the LiCl-free electrolyte and ~50 mAh g_S^{-1} in the LiCl-saturated electrolyte. These capacities are negligible compared with the total capacity of the S–LiCl electrode, indicating that Cl^- species originating only from the electrolyte are insufficient to sustain substantial sulfur oxidation. Instead, the electrochemical activity of the S–LiCl electrode relies primarily on the gradual dissolution and utilization of LiCl embedded within the electrode itself. In this mechanism, free Cl^- species in the electrolyte

initiate sulfur oxidation, while LiCl within the electrode continuously dissolves to replenish the Cl^- consumed during cycling. As a result, the overall Cl^- concentration in the electrolyte remains approximately constant during operation.

To support this mechanism, Scanning electron microscopy (SEM)/energy-dispersive X-ray spectroscopy (EDS) analyses were performed on S–LiCl electrodes recovered at different voltages (2.6, 3.2, and 3.6 V) in the LiTFSI–EMIMCl–TTE electrolyte (**Supplementary Figures 37–39**). At 2.6 and 3.2 V, needle-like LiCl crystals are clearly observed by EDS mapping. Compared with the pristine electrode (**Supplementary Figure 2**), these LiCl particles exhibit substantial morphological changes, indicating a dissolution–recrystallization process during cycling. The persistence of undissolved LiCl at intermediate voltages further confirms that the electrolyte alone does not fully dissolve LiCl within the electrode. After charging to 3.6 V, S, Cl, and C become uniformly distributed and no apparent crystalline LiCl particles are observed, indicating the formation of S_2Cl_2 within the carbon matrix and substantial consumption of electrochemically accessible LiCl.

The LiTFSI–EMIMCl–TTE electrolyte therefore functions primarily as a chlorine mediator rather than a major energy-storage component. Based on the measured electrochemical response of S–C electrodes, the direct energy contribution from the electrolyte is estimated to be ~2–3% of the total cell energy. Therefore, calculating the energy density of the Li||S–LiCl system based on the electrode materials alone is justified and allows meaningful comparison with other battery chemistries.

Supplementary Figures

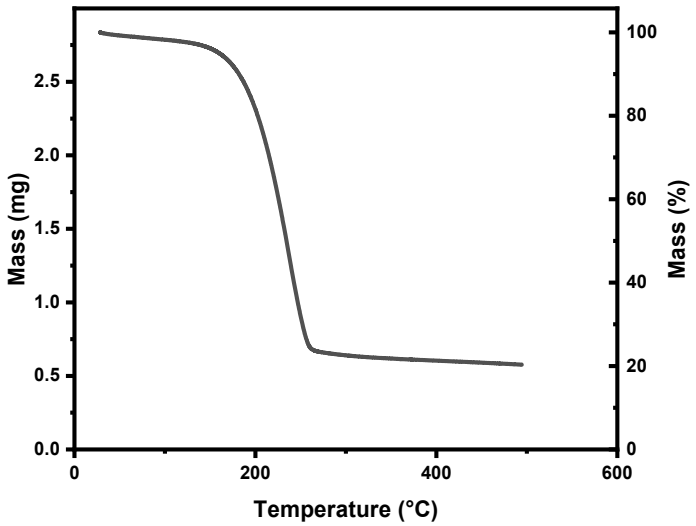

Supplementary Figure 1. Thermogravimetric analysis curve of the S–C electrode measured at a heating rate of 5 °C min^{-1} from 25 °C to 500 °C. The sulfur content of the S–C composite is ~80 wt%.

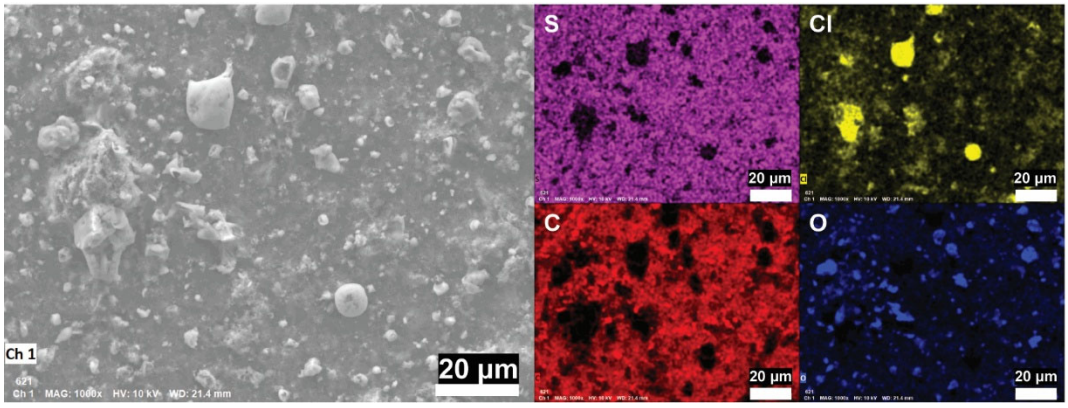

Supplementary Figure 2. SEM image and corresponding EDS elemental mappings of S, Cl, C, and O for the pristine S–LiCl electrode.

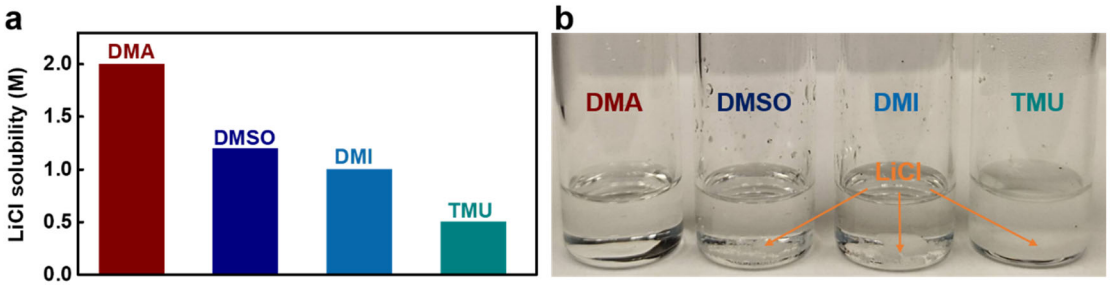

Supplementary Figure 3. a, Solubility of LiCl in different solvents, including N,N-dimethylacetamide (DMA), dimethyl sulfoxide (DMSO), 1,3-dimethyl-2-imidazolidinone (DMI), and tetramethylurea (TMU). **b,** Photographs of 2 M LiCl solutions in the corresponding solvents.

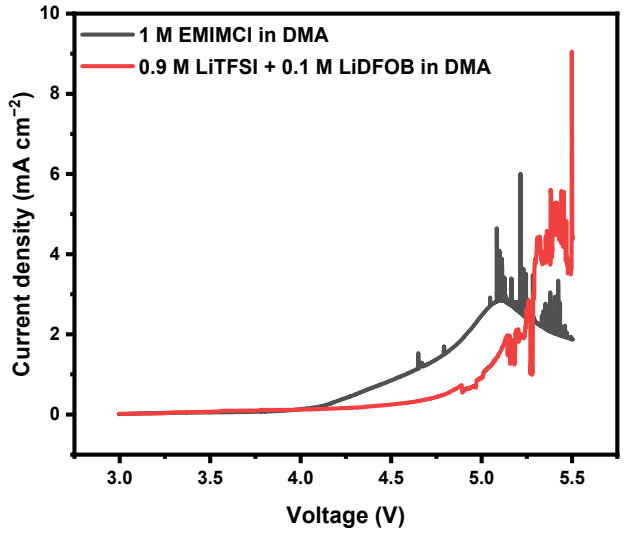

Supplementary Figure 4. Linear sweep voltammetry (LSV) curves of the 1 M EMIMCl/DMA electrolyte and the 0.9 M LiTFSI + 0.1 M LiDFOB in DMA electrolyte measured in Li||Al cells.

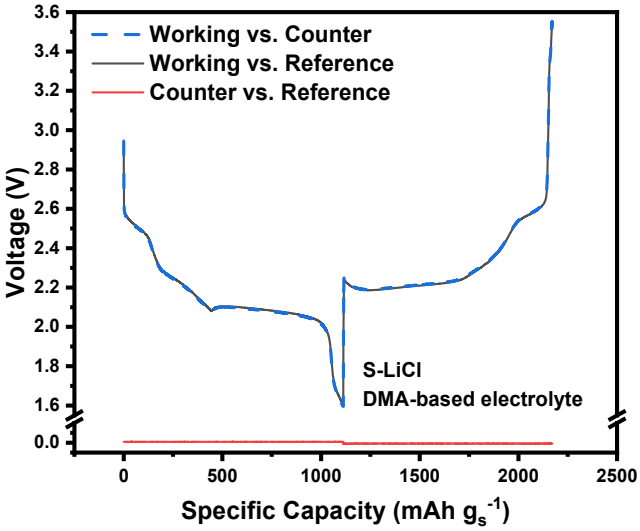

Supplementary Figure 5. Three-electrode measurements of the Li||S–LiCl cell in the DMA-based electrolyte. The blue dashed line denotes the working electrode versus counter electrode trace; the grey solid line denotes the working electrode versus reference electrode trace; and the red solid line denotes the counter electrode versus reference electrode trace. The blue and grey traces nearly overlap because separate Li metal electrodes are used as the counter and reference electrodes.

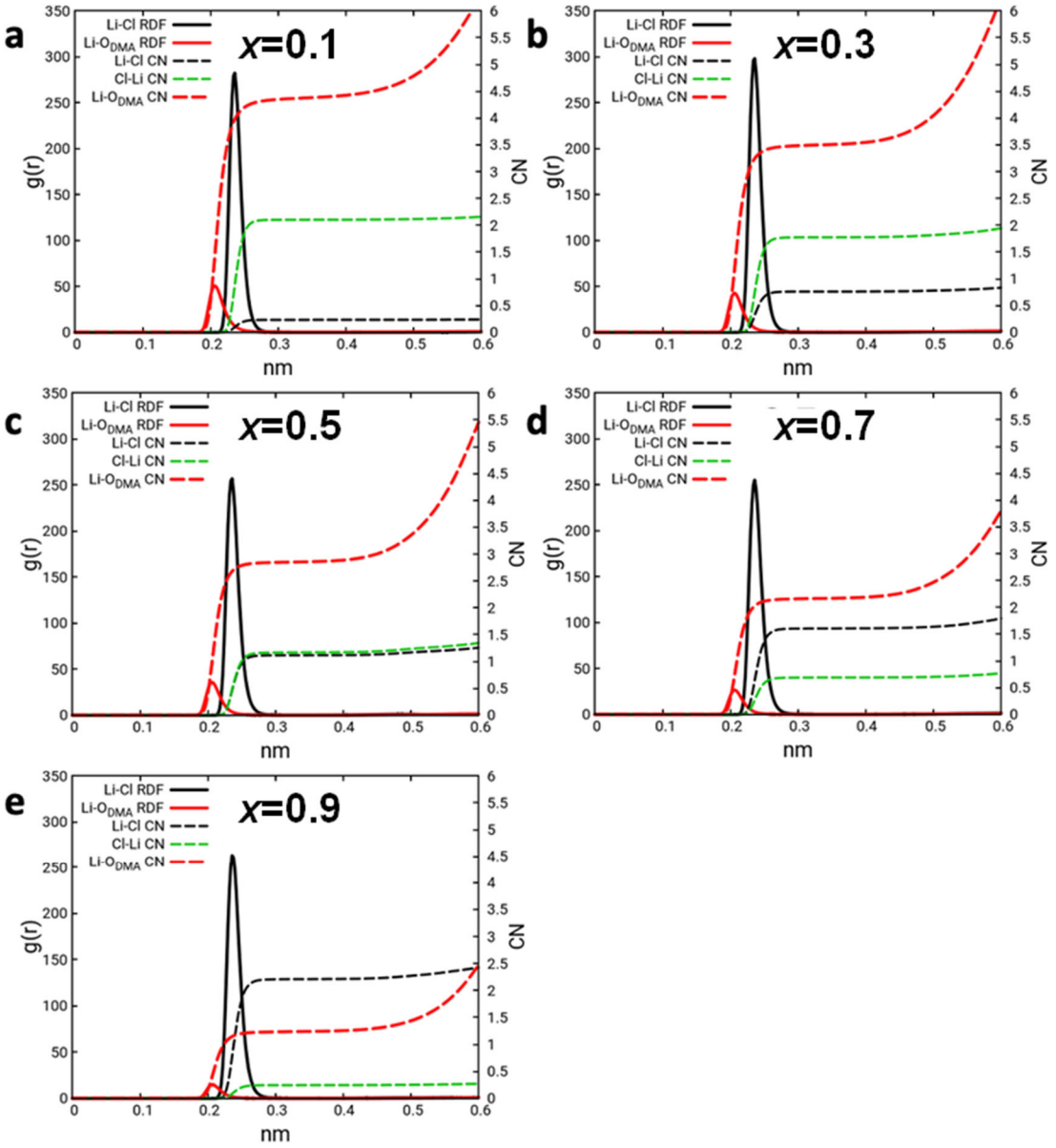

Supplementary Figure 6. Radial distribution functions and coordination numbers obtained from molecular dynamics simulations for DMA-based electrolytes containing (1−*x*) M LiTFSI and *x* M EMIMCl. **a,** *x* = 0.1; **b,** *x* = 0.3; **c,** *x* = 0.5; **d,** *x* = 0.7; **e,** *x* = 0.9.

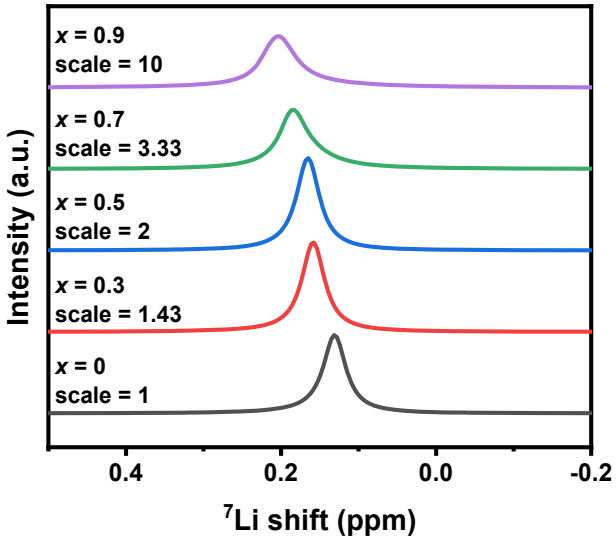

Supplementary Figure 7. ^{7}Li nuclear magnetic resonance (NMR) spectra of DMA-based electrolytes containing (1−*x*) M LiTFSI and *x* M EMIMCl, with *x* = 0, 0.3, 0.5, 0.7, and 0.9.

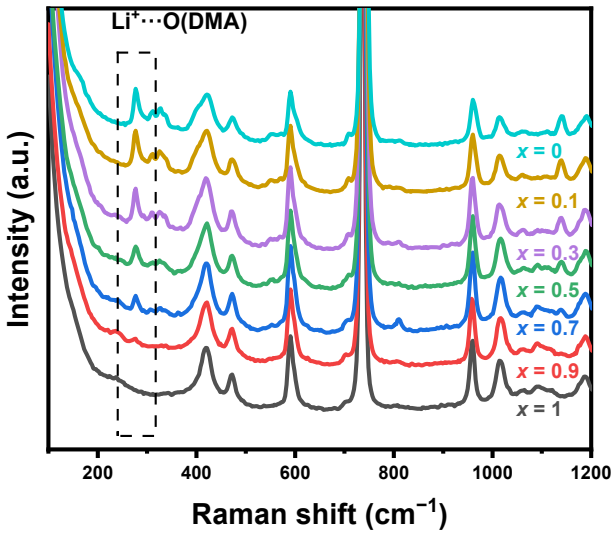

Supplementary Figure 8. Raman spectra of DMA-based electrolytes containing (1−*x*) M LiTFSI and *x* M EMIMCl, with *x* = 0, 0.1, 0.3, 0.5, 0.7, 0.9, and 1. The dashed box indicates the Li^{+}–O(DMA) region.

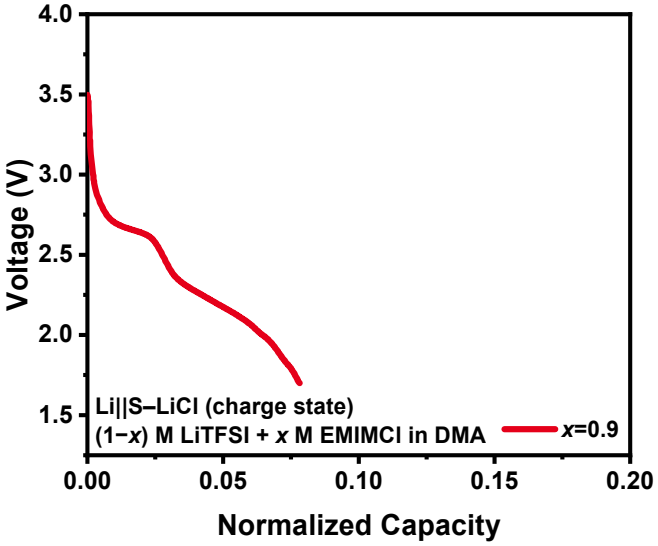

Supplementary Figure 9. Discharge profile of the fully charged S–LiCl electrode in a DMA-based electrolyte containing 0.1 M LiTFSI and 0.9 M EMIMCl after the first charge.

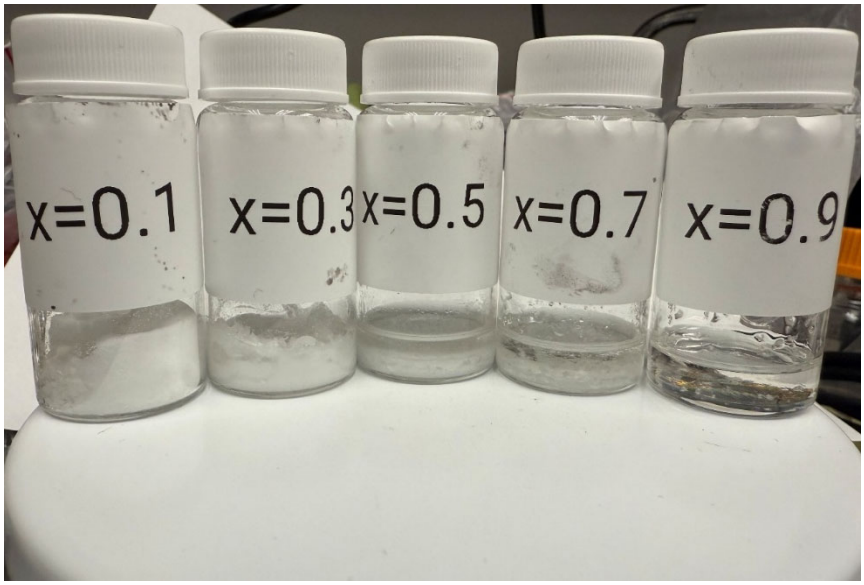

Supplementary Figure 10. Photographs of LiTFSI–EMIMCl mixtures heated on a 45 °C hotplate, with compositions denoted as (1−*x*) LiTFSI–*x* EMIMCl.

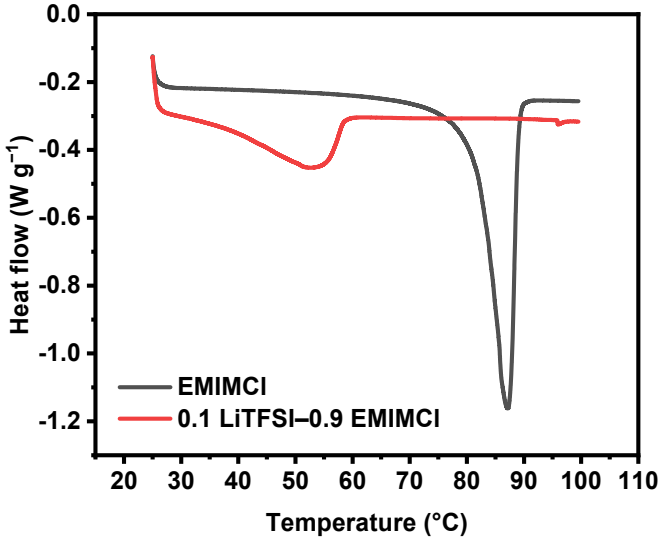

Supplementary Figure 11. Differential scanning calorimetry (DSC) profiles of EMIMCl and 0.1 LiTFSI–0.9 EMIMCl recorded in the temperature range of 25–100 °C at a heating rate of 2 °C min^{-1}.

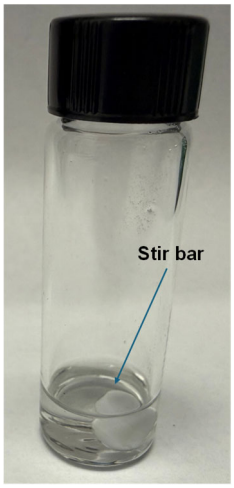

Supplementary Figure 12. Photograph of the LiTFSI–EMIMCl–TTE electrolyte. The arrow indicates the stir bar.

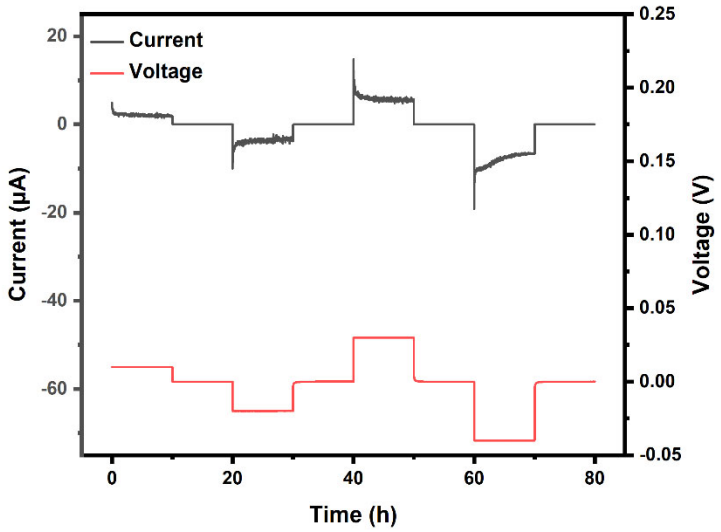

Supplementary Figure 13. Voltage and current profiles of a Li||Li symmetric cell using the LiTFSI–EMIMCl–TTE (1:9:10) electrolyte. Potentiostatic polarization was sequentially applied at +10, −20, +30, and −40 mV, with each step maintained for 10 h, followed by a 10 h relaxation period.

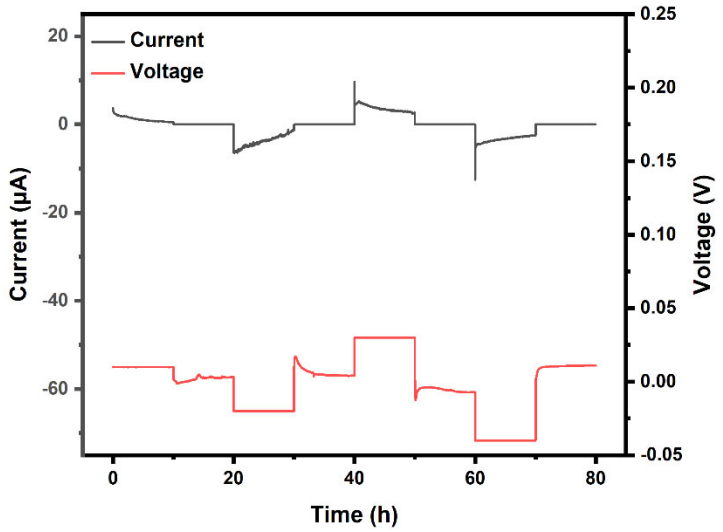

Supplementary Figure 14. Voltage and current profiles of a Li||Li symmetric cell using the LiTFSI–EMIMCl (1:9) electrolyte. Potentiostatic polarization was sequentially applied at +10, −20, +30, and −40 mV, with each step maintained for 10 h, followed by a 10 h relaxation period.

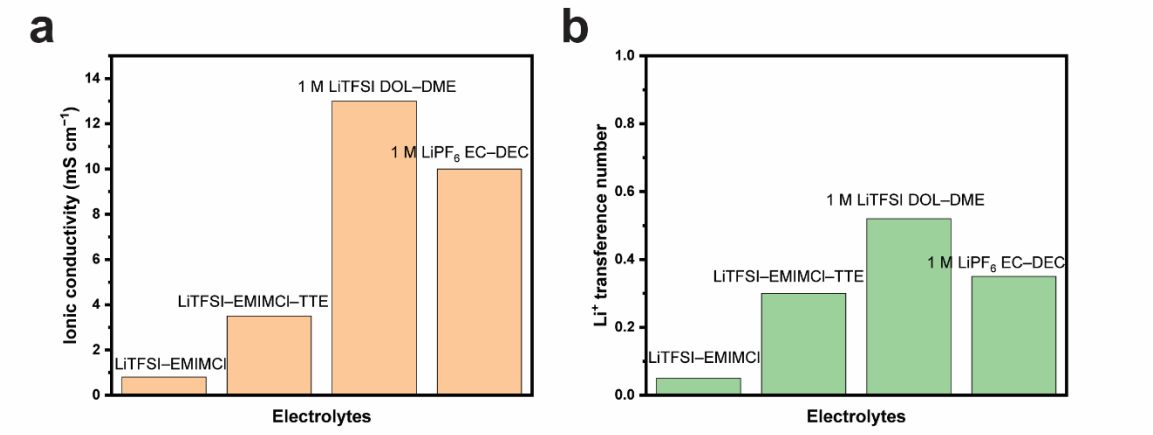

Supplementary Figure 15. a, Ionic conductivity and **b,** Li^+ transference numbers of various electrolytes, including LiTFSI–EMIMCl (1:9), LiTFSI–EMIMCl–TTE (1:9:10), 1 M LiTFSI in 1,3-dioxolane (DOL)–1,2-dimethoxyethane (DME), and 1 M $LiPF_6$ in ethylene carbonate (EC)–diethyl carbonate (DEC).

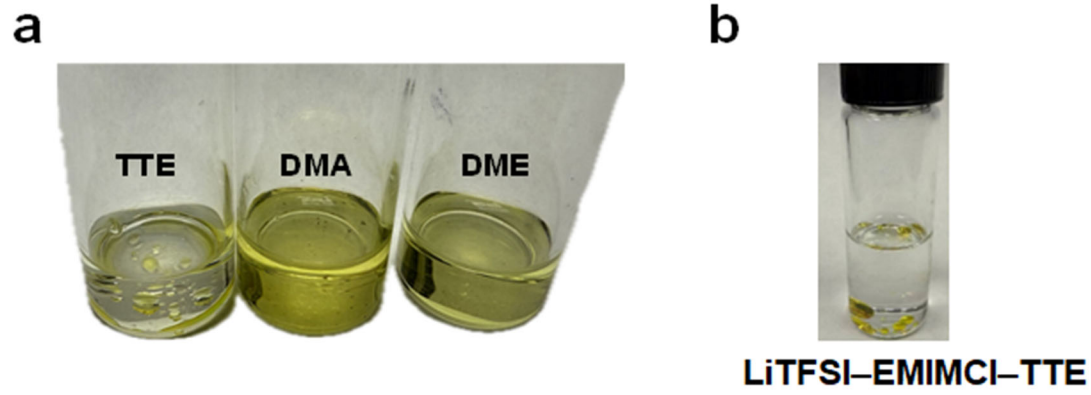

Supplementary Figure 16. a, Photographs of S_2Cl_2 mixed with different solvents, including TTE, DMA, and DME. **b,** Photograph of S_2Cl_2 mixed with the LiTFSI–EMIMCl–TTE electrolyte.

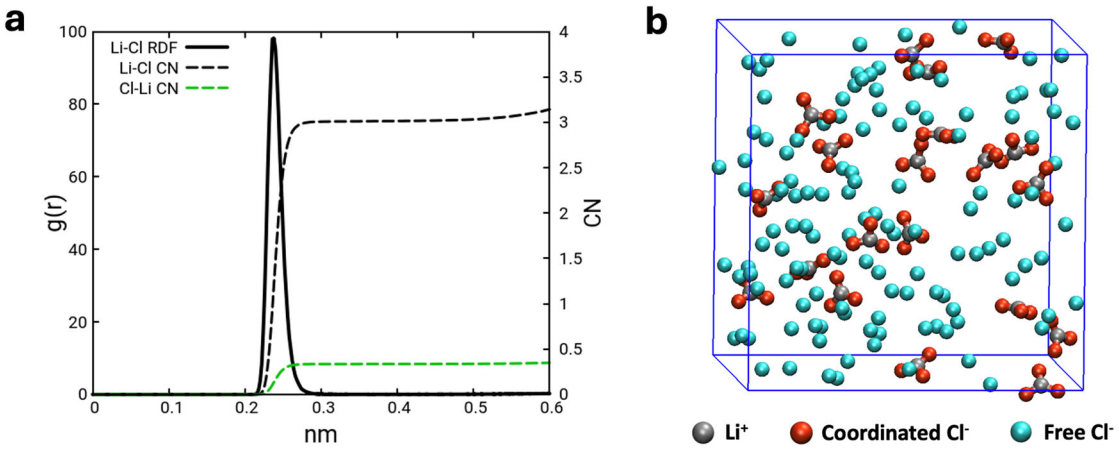

Supplementary Figure 17. Molecular dynamics simulations of the LiTFSI–EMIMCl–TTE (1:9:10) electrolyte: **a,** Li–Cl radial distribution functions and coordination numbers; **b,** representative snapshot of the electrolyte structure.

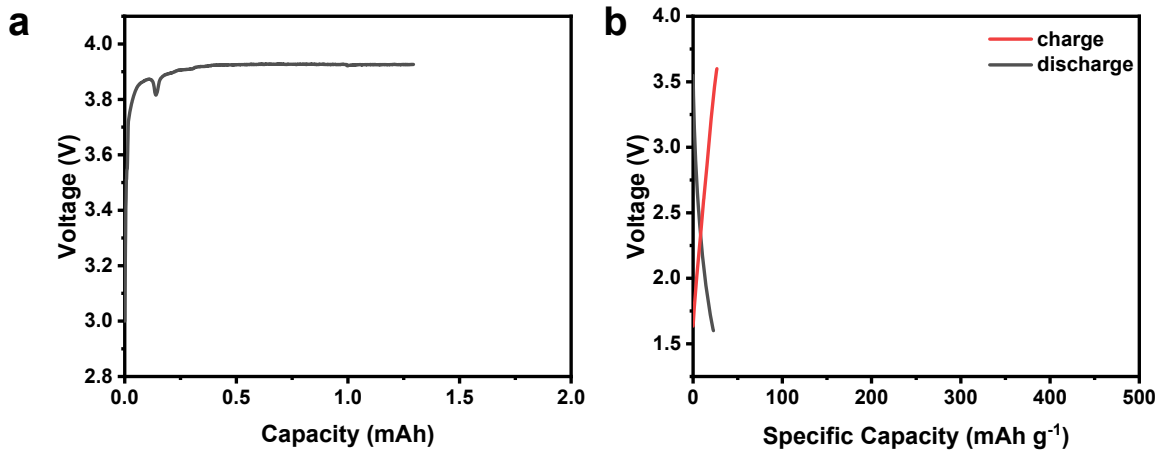

Supplementary Figure 18. a, Charging voltage profiles of Li||Al cells using the LiTFSI–EMIMCl–TTE electrolyte. **b,** Charge/discharge voltage profiles of carbon electrodes versus Li metal using the LiTFSI–EMIMCl–TTE electrolyte.

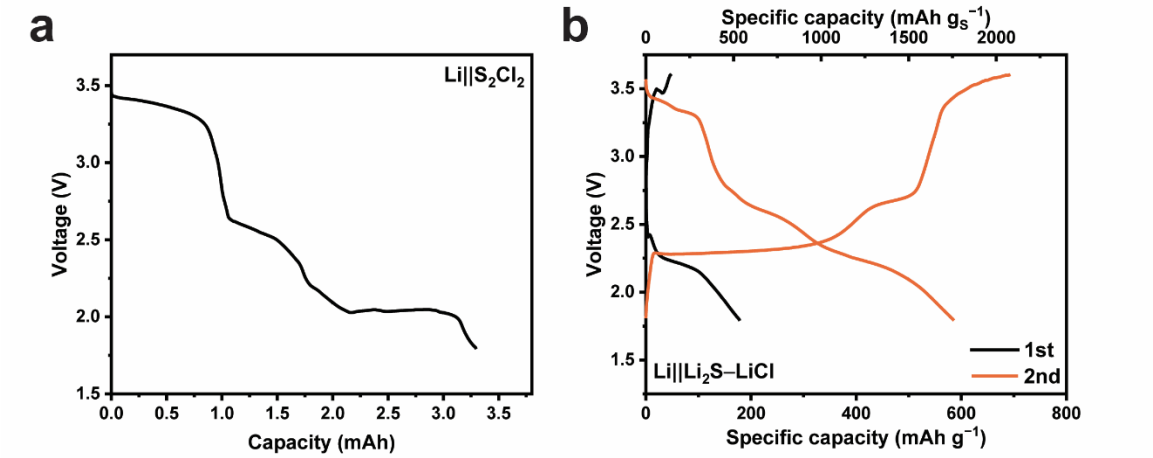

Supplementary Figure 19. a, Voltage profile of the Li||S_2Cl_2 cell. **b,** First-cycle (activation) and second-cycle voltage profiles of the Li||Li_2S–LiCl cell with initial charging.

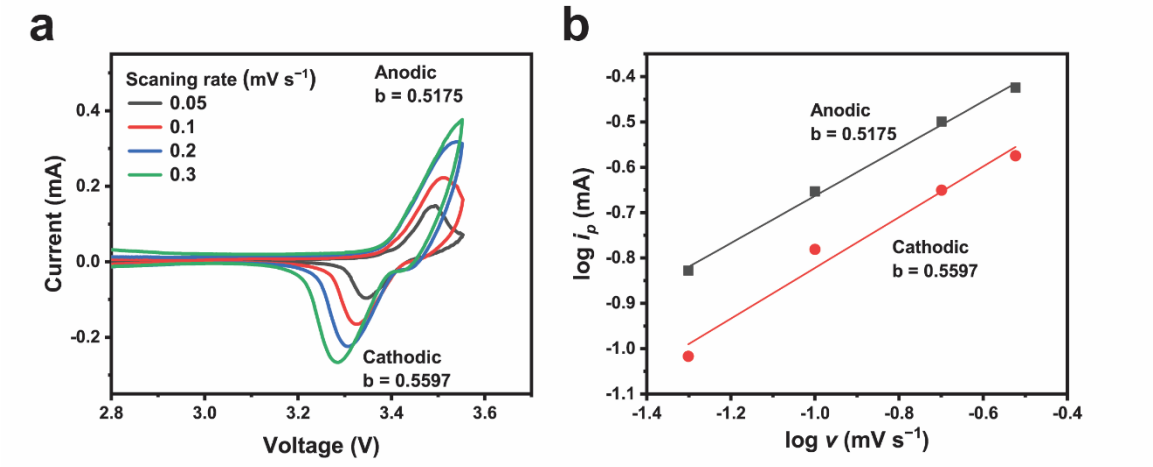

Supplementary Figure 20. a, Cyclic voltammetry (CV) curves of the Li||S–LiCl cell in the LiTFSI–EMIMCl–TTE electrolyte recorded between 2.8 V and 3.6 V at scan rates of 0.05, 0.1, 0.2, and 0.3 mV s^{-1}. **b,** Corresponding plots of log i_p versus log v for the anodic and cathodic peaks.

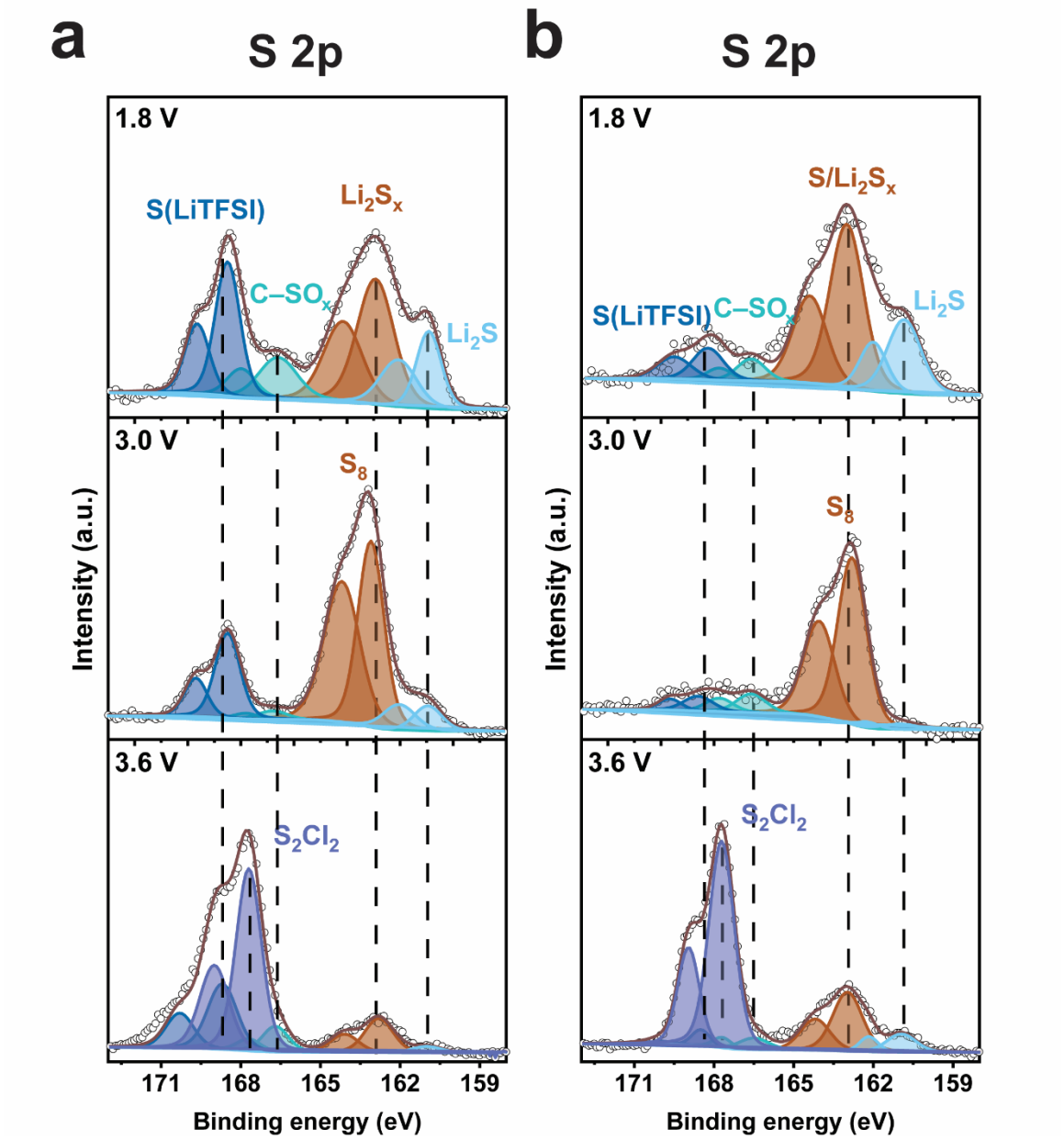

Supplementary Figure 21. XPS analysis of S 2p spectra of S–LiCl electrodes in the LiTFSI–EMIMCl–TTE electrolyte after being held at 1.8, 3.0, and 3.6 V for 4 h: **a,** outermost surface; **b,** surface after 600 s of Ar sputtering.

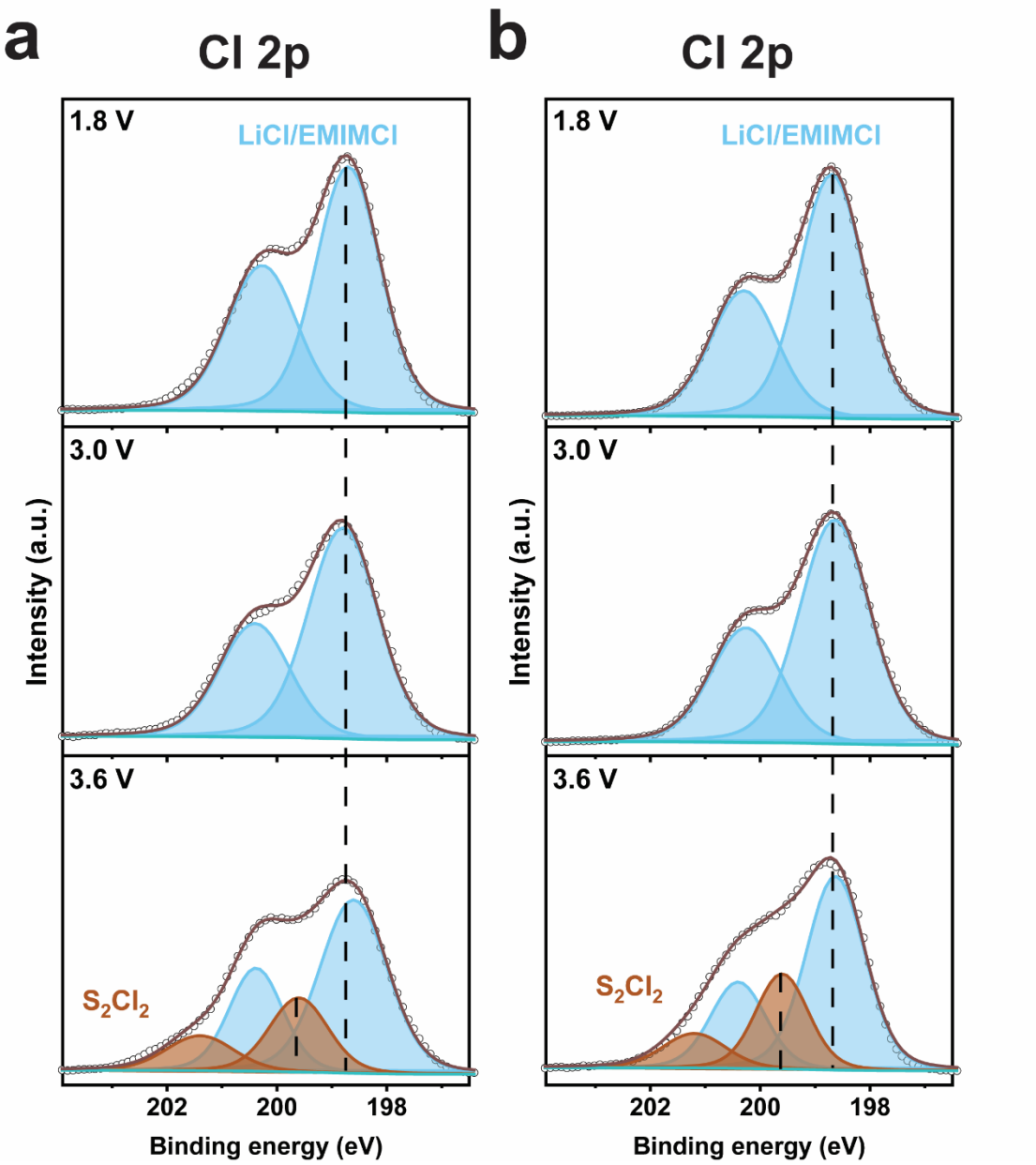

Supplementary Figure 22. XPS analysis of Cl 2p spectra of S–LiCl electrodes in the LiTFSI–EMIMCl–TTE electrolyte after being held at 1.8, 3.0, and 3.6 V for 4 h: **a,** outermost surface; **b,** surface after 600 s of Ar sputtering.

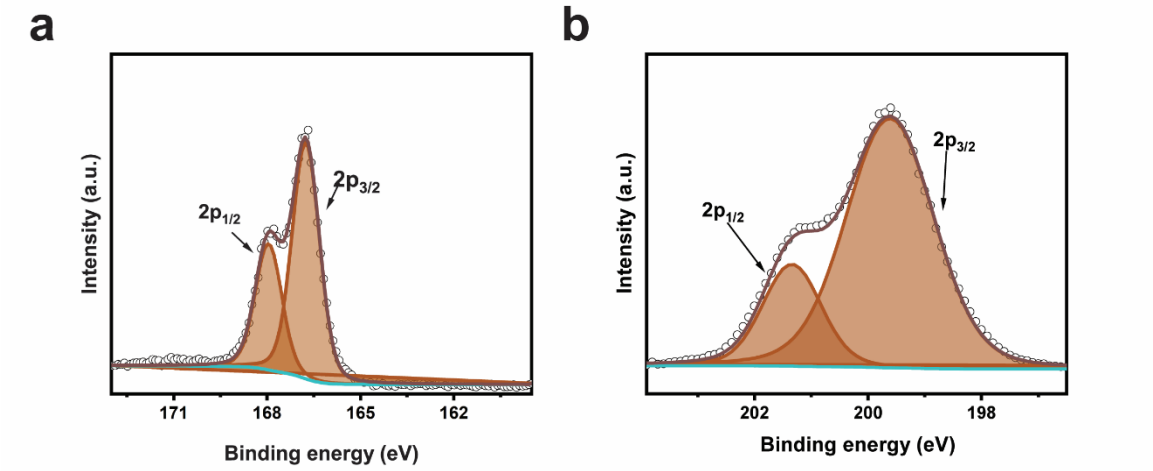

Supplementary Figure 23. XPS spectra of the S_2Cl_2 reference sample mixed with carbon: **a,** S 2p region; **b,** Cl 2p region.

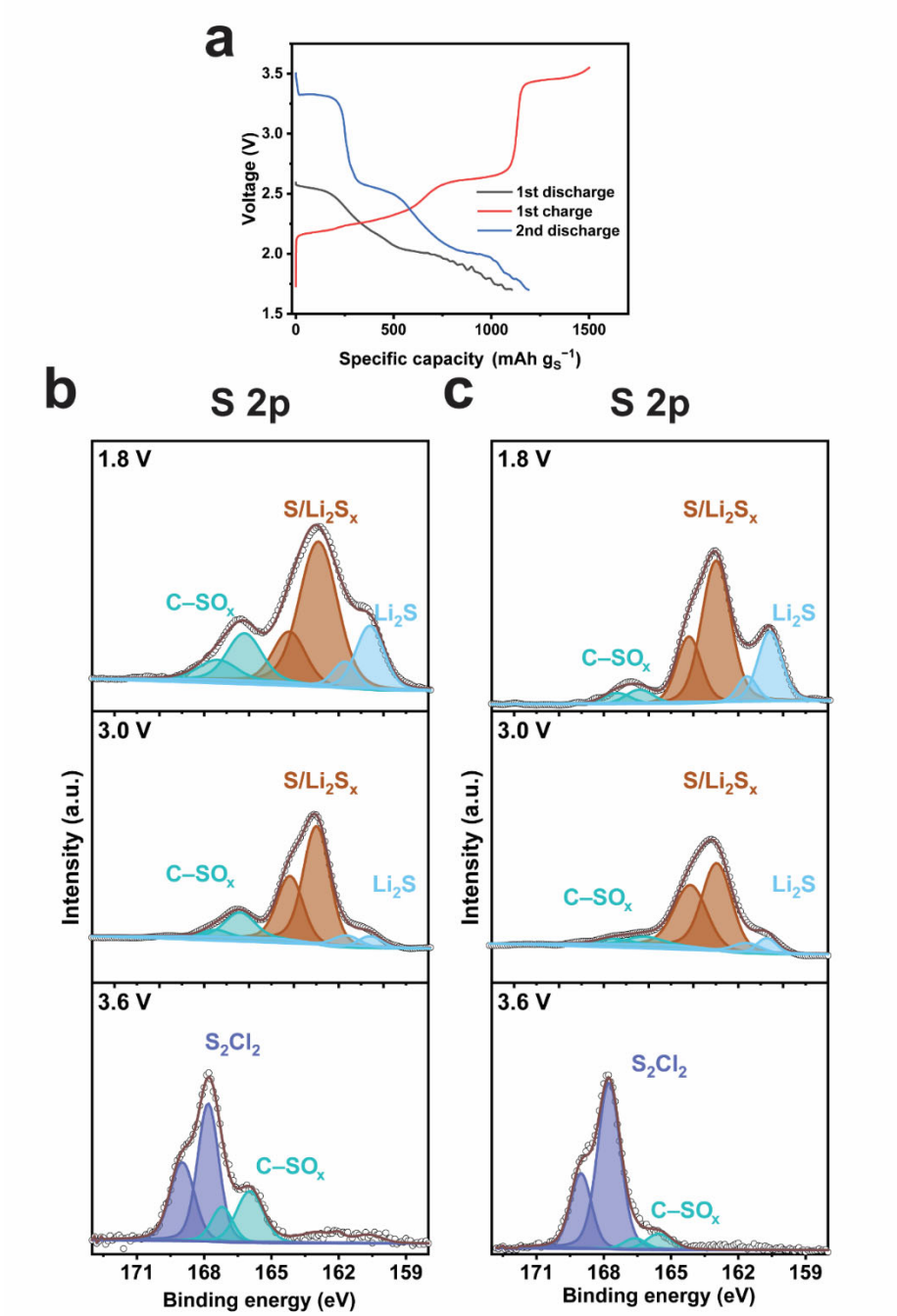

Supplementary Figure 24. **a,** First-discharge, first-charge, and second-discharge voltage profiles of the S–LiCl electrode in the $LiPF_6$–EMIMCl–TTE electrolyte. **b,c,** XPS analysis of S 2p spectra of S–LiCl electrodes in the $LiPF_6$–EMIMCl–TTE electrolyte after being held at 1.8, 3.0, and 3.6 V for 4 h: **b,** outermost surface; **c,** surface after 600 s of Ar sputtering.

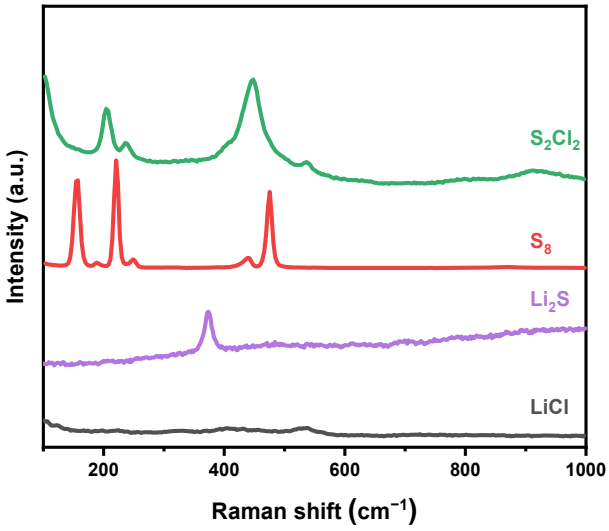

Supplementary Figure 25. Raman spectra of the reference materials S_2Cl_2, S_8, Li_2S, and LiCl.

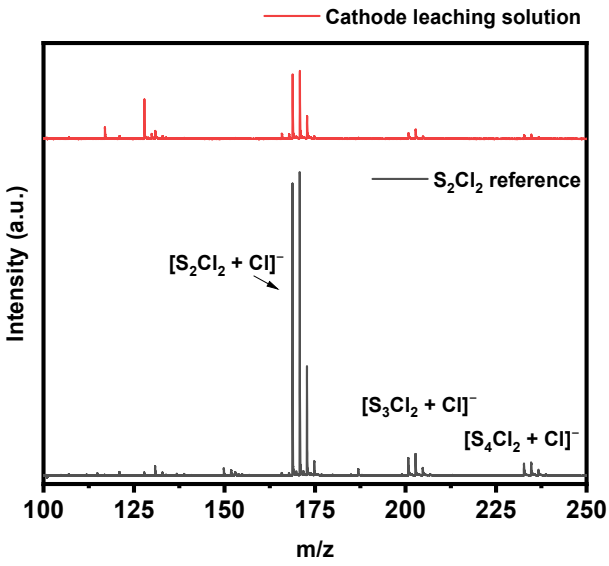

Supplementary Figure 26. Direct analysis in real time mass spectrometry (DART–MS) spectra of the S_2Cl_2 reference sample and the cathode supernatant extracted from the fully charged cathode.

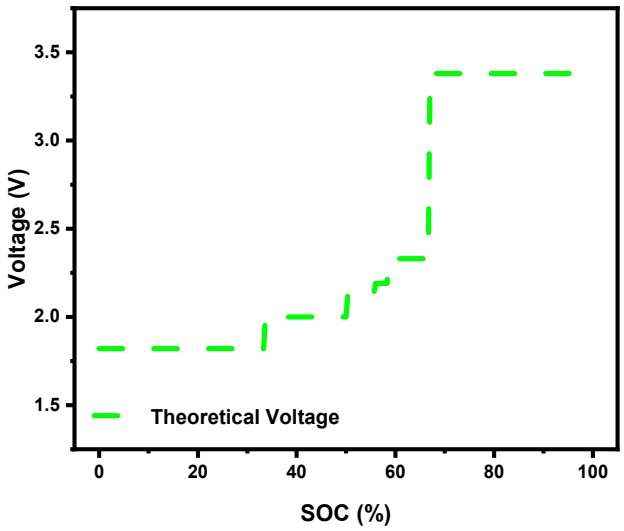

Supplementary Figure 27. Theoretical voltage profiles of the Li||S_2Cl_2 chemistry corresponding to the multistep sulfur redox reactions.

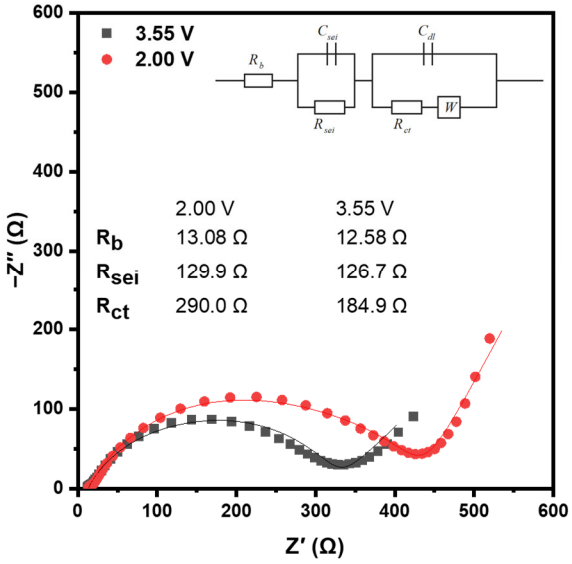

Supplementary Figure 28. Nyquist plots and corresponding fitted results of the Li||S–LiCl cell measured at 3.55 V and 2.00 V immediately after reaching the target voltages. The inset shows the equivalent-circuit model used for fitting.

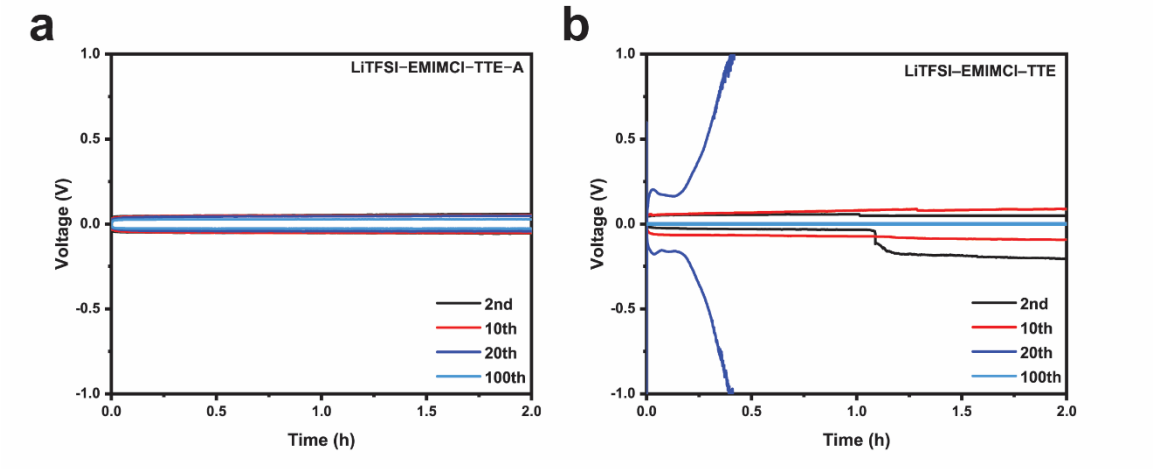

Supplementary Figure 29. Voltage profile of Li||Li symmetric cells at 25 °C. The current density is 0.2 mA cm^{-2}. **a,** LiTFSI–EMIMCl–TTE–A electrolyte; **b,** LiTFSI–EMIMCl–TTE electrolyte.

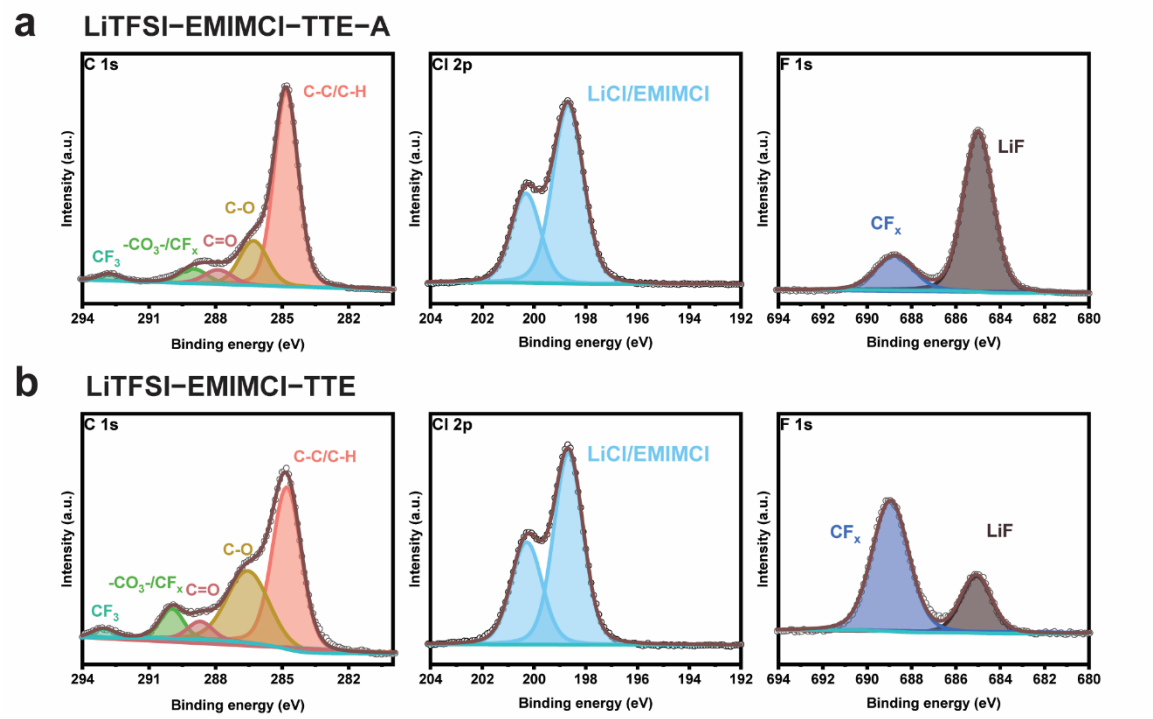

Supplementary Figure 30. XPS spectra of the C 1s, F 1s, and Cl 2p regions of lithium metal surfaces after cycling in **a,** LiTFSI–EMIMCl–TTE–A and **b,** LiTFSI–EMIMCl–TTE electrolytes.

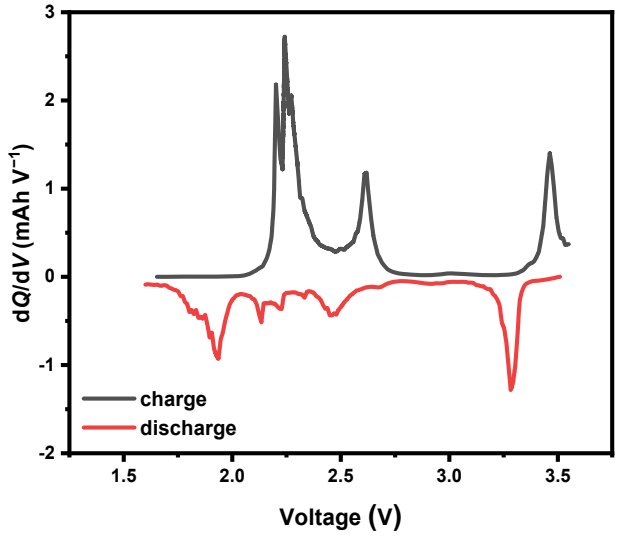

Supplementary Figure 31. Differential capacity (dQ/dV) profile of the Li||S–LiCl cell in the LiTFSI–EMIMCl–TTE–A electrolyte during the 5th cycle.

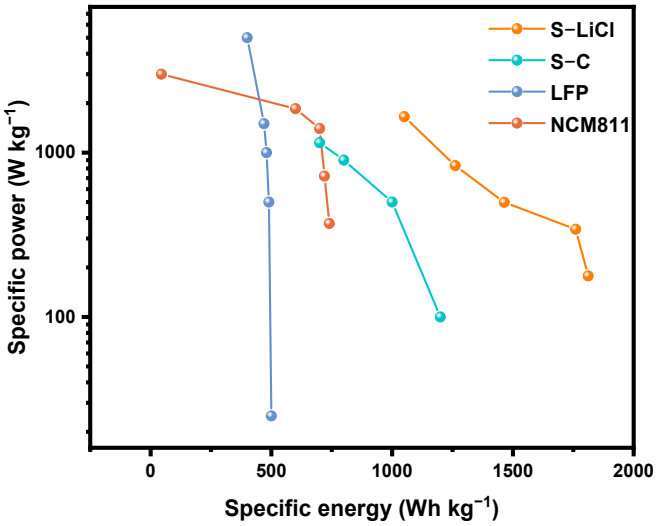

Supplementary Figure 32. Ragone plots of S–LiCl, S–C, $LiFePO_4$ (LFP), and $LiNi_{0.8}Co_{0.1}Mn_{0.1}O_2$ (NCM811) electrodes, showing the relationship between specific energy and specific power at different discharge rates.

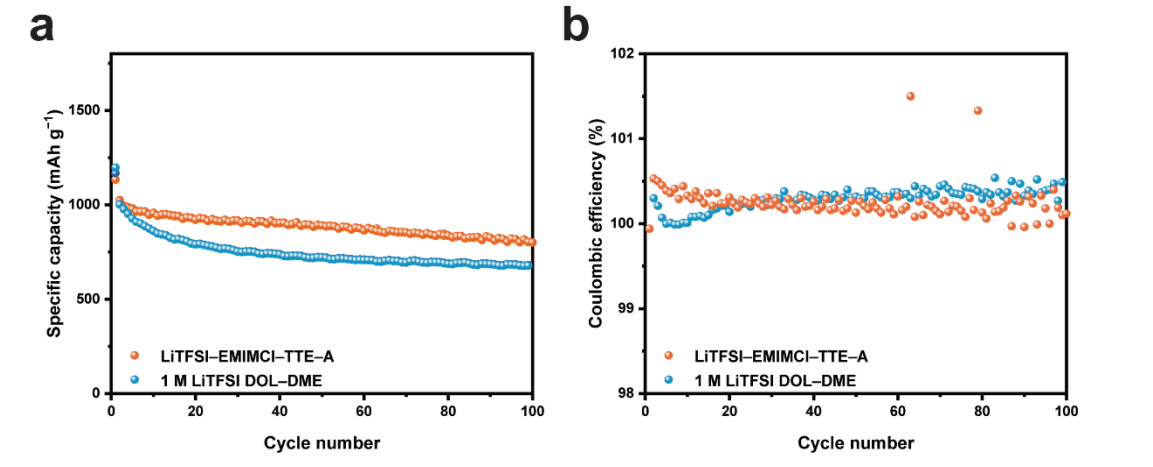

Supplementary Figure 33. Cycling performance of S–C electrodes in LiTFSI–EMIMCl–TTE–A and 1 M LiTFSI in DOL–DME electrolytes: **a,** specific capacity; **b,** coulombic efficiency.

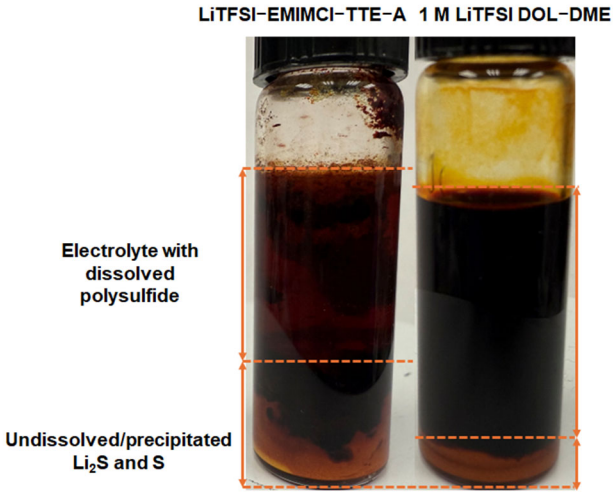

Supplementary Figure 34. Photographs showing the dissolution behavior of 1.5 M Li_2S_6 in LiTFSI–EMIMCl–TTE–A (left) and 1 M LiTFSI in DOL–DME (right). Li_2S_6 was prepared by mixing elemental sulfur and Li_2S, followed by stirring and heating at 60 °C before being cooled to room temperature for imaging.

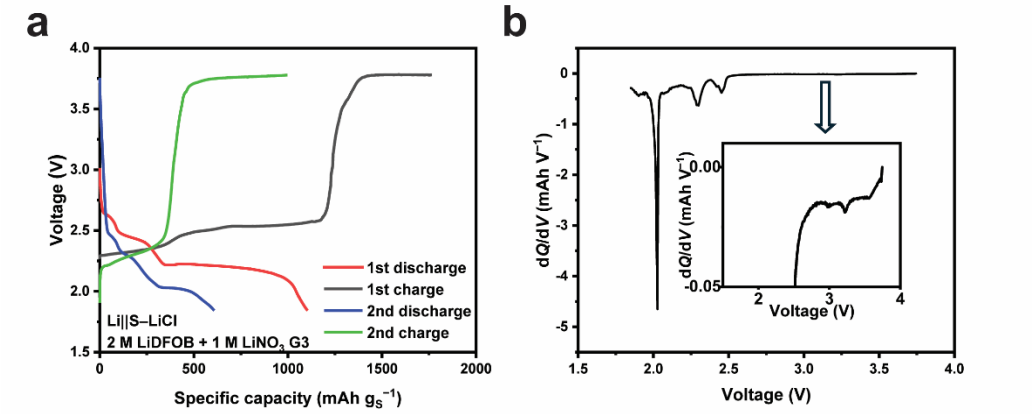

Supplementary Figure 35. a, First-cycle and second-cycle charge/discharge voltage profiles of the S–LiCl electrode in the G3-based electrolyte. **b,** dQ/dV profile of the second discharge cycle (inset: magnified view near 3.2–3.3 V).

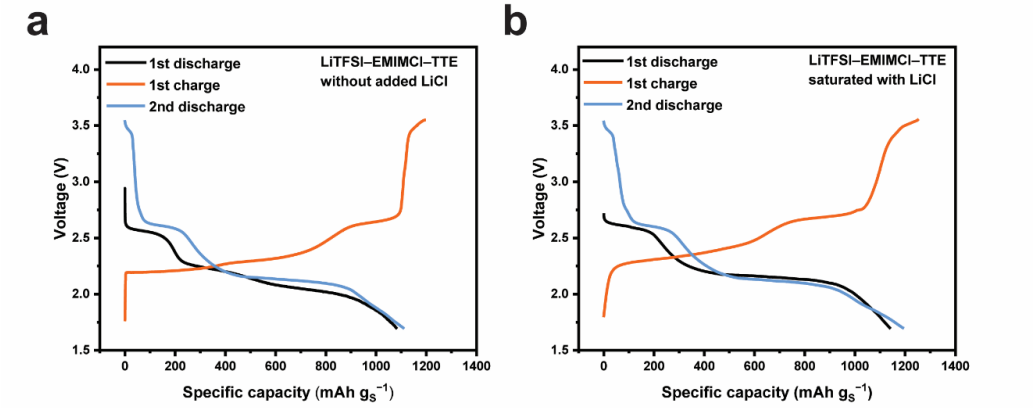

Supplementary Figure 36. Charge/discharge voltage profiles of the S–C electrode in **a,** LiTFSI–EMIMCl–TTE and **b,** LiTFSI–EMIMCl–TTE saturated with LiCl.

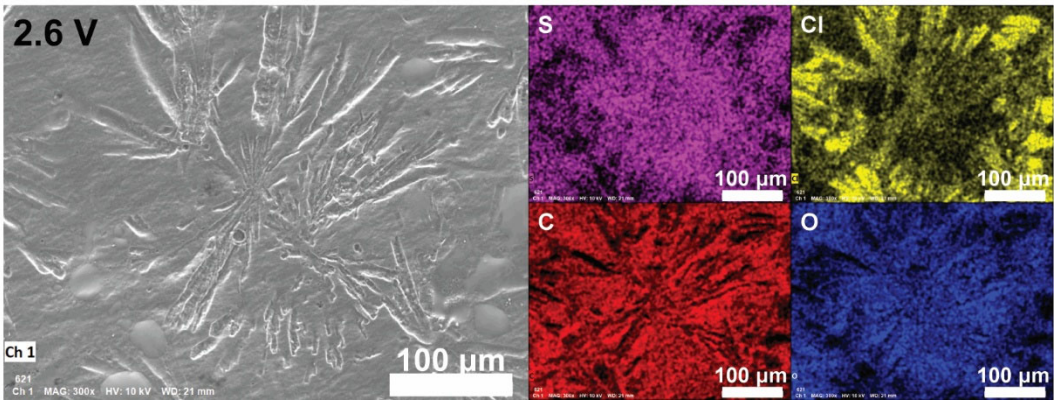

Supplementary Figure 37. SEM image and corresponding EDS elemental mappings of S, Cl, C, and O for the S–LiCl electrode at 2.6 V in the LiTFSI–EMIMCl–TTE electrolyte.

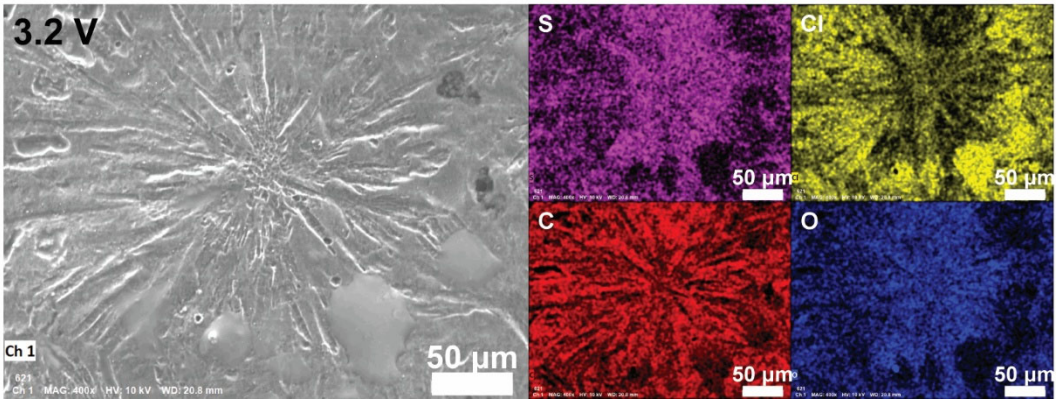

Supplementary Figure 38. SEM image and corresponding EDS elemental mappings of S, Cl, C, and O for the S–LiCl electrode at 3.2 V in the LiTFSI–EMIMCl–TTE electrolyte.

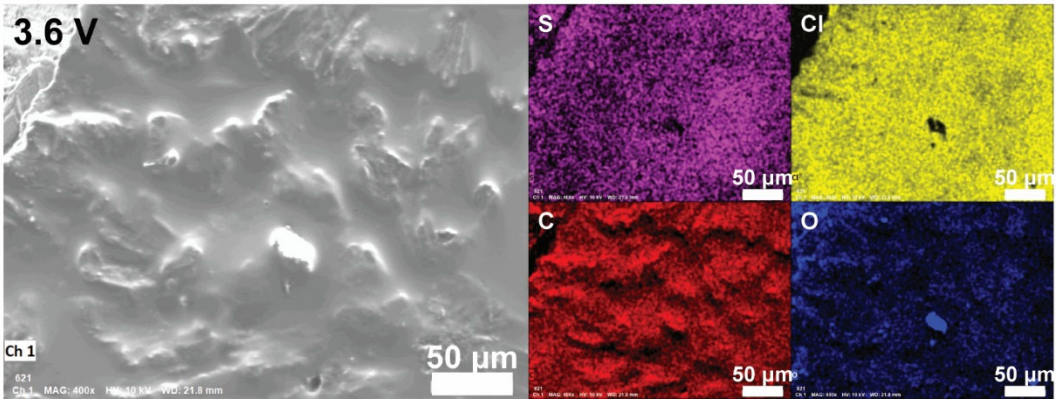

Supplementary Figure 39. SEM image and corresponding EDS elemental mappings of S, Cl, C, and O for the S–LiCl electrode at 3.6 V in the LiTFSI–EMIMCl–TTE electrolyte.

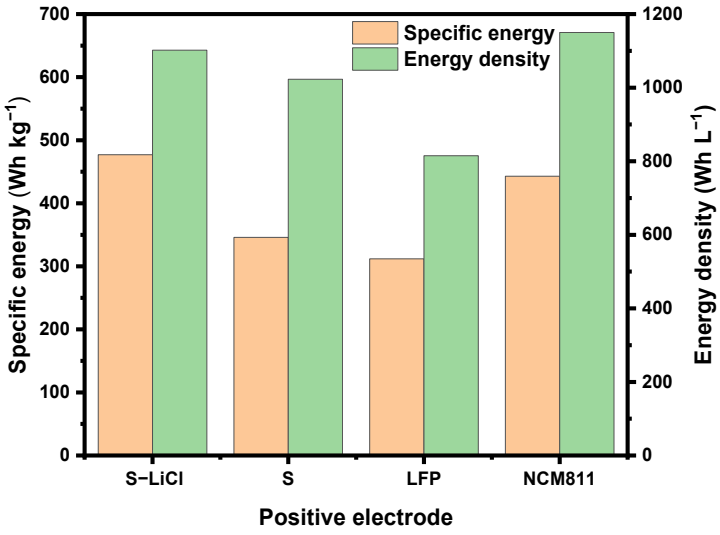

Supplementary Figure 40. Comparison of the stack-level specific energies and energy densities of cells using S–LiCl, S, LFP, and NCM811 positive electrodes.

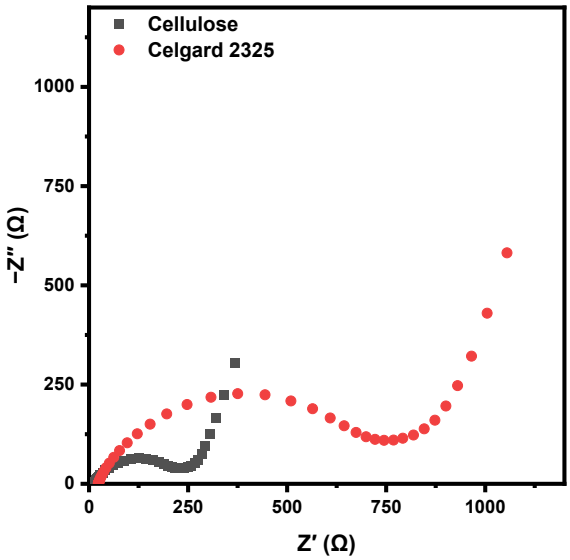

Supplementary Figure 41. Electrochemical impedance spectroscopy (EIS) Nyquist plots of Li||S–LiCl cells assembled with cellulose separators and Celgard 2325 separators.

Supplementary Tables

Supplementary Table 1. High-throughput calculations of the theoretical energy densities of binary conversion electrodes, sorted by theoretical specific energy. Values in parentheses indicate systems for which significant deviations between calculated and experimental data may exist.

Compound	Specific Capacity ($mAh\ g^{-1}$)	Average Voltage (V)	Specific Energy ($Wh\ kg^{-1}$)
F_2	1030	(6.09)	(6277)
OF_2	1307	(4.54)	(5935)
O_2	1792	(2.91)	(5216)
ClF_5	932	(5.14)	(4794)
NF_3	1423	(3.17)	(4510)
SF_6	1061	(3.52)	(3736)
NO_3	1929	(1.87)	(3608)
SO_3	1576	(2.28)	(3594)
BrF_5	741	4.7	3484
BrO_3	1060	3.12	3308
SeF_4	816	3.52	2874
Cl_2O_7	897	3.18	2853
IF_7	678	(3.98)	(2701)
S	1167	2.28	2661
NCl_3	990	2.59	2564
PF_5	1178	(2.17)	(2556)
Cl_2	631	(3.98)	(2512)
SeO_2	1050	2.31	2427
S_2Cl_2	910	2.65	2412
SeS_7	1034	2.28	2358
SN	1658	1.42	2354
P_2S_7	1260	1.85	2332
SCl_2	820	2.75	2255
TeF_6	720	(3.12)	(2247)

BrN	880	2.3	2025
PCl_5	811	2.4	1947
CoF_3	587	3.22	1891
$SeCl_4$	611	3.09	1890
TeS_3	767	2.46	1888
I_2O_5	771	2.44	1881
TeO_3	925	1.96	1814
P	1552	1.07	1660
CoO_2	782	2.11	1651
FeF_3	600	2.74	1646
CuF_2	464	3.5	1624
MnO_2	932	1.71	1595
S_2Br_2	605	2.63	1592
SeN	1049	1.44	1511
TeN_2	1015	1.41	1432
$TeCl_4$	516	2.71	1399
BrCl	414	3.36	1391
PSe	926	1.48	1371
FeS_2	725	1.85	1342
Fe_2O_3	796	1.63	1298
CuO	573	2.24	1284
IN	635	2	1270
Se	577	2.18	1259
ICl_3	410	3.02	1238
$FeCl_3$	438	2.82	1237
N_2	2310	0.53	1224
$LiMnF_4$	513	2.26	1159
MnP_4	1227	0.93	1141
$CuCl_2$	360	3.14	1133
FeP_4	1222	0.92	1124
P_3N_5	1952	0.57	1112

SI	447	2.45	1095
Br_2	308	3.54	1092
CoS	510	2.01	1027
PBr_7	406	2.5	1015
$TeSe_2$	491	2.03	997
CuS	489	2.01	983
CoP_3	1125	0.86	967
$CoCl_2$	372	2.58	961
TeP	693	1.35	935
$TeBr_6$	323	2.79	902
$SeBr_4$	365	2.47	902
P_2O_5	676	1.28	866
$CoSe_2$	438	1.92	841
IBr_2	261	2.92	763
$FeSe_2$	443	1.67	741
SeI_2	297	2.32	689
CuSe	342	1.99	681
Te	378	1.77	670
PI_2	419	1.55	650
$MnCl_2$	383	1.69	647
MnS	531	1.16	616
$CoBr_2$	230	2.46	566
I_2	200	2.79	558
FeN	886	0.62	549
$FeBr_2$	233	2.32	541
TeI_7	223	2.32	518
CoN	856	0.6	513
$CoTe_2$	313	1.62	507
Cu_3N	356	1.3	463
$MnTe_2$	317	1.45	460
$FeTe_2$	316	1.42	449

MnSe	362	1.23	446
CuBr	178	2.5	445
CuTe	261	1.68	439
CoI_2	164	2.37	388
FeI_2	165	2.21	366
$MnBr_2$	234	1.5	351
Cu_3P	331	1.04	344
MnN	895	0.37	331
CuI	135	2.07	281
MnI_2	166	1.68	279

Supplementary Table 2. Stack-level specific energy and energy density calculations for the Li||S–LiCl cell.

		S–LiCl	S–C	$LiFePO_4$	NCM811
Positive Electrode					
Specific Capacity	mAh g^{-1}	713.4	960	145	200
Average Voltage	V	2.54	2.05	3.4	3.7
Loading	mg cm^{-2}	6.23	4.63	30.65	22.2
Density	g cm^{-3}	2.08	1.96	3.47	3.5
Porosity	%	50%	50%	35%	35%
Thickness	μm	59.9	47.2	135.9	97.6
Active Mat. Percentage	%	90%	90%	90%	90%
Areal Capacity	mAh cm^{-2}	4.00	4.00	4.00	4.00
Negative Electrode					
Specific Capacity	mAh g^{-1}	3861	3861	3861	3861
Average Voltage	V	0	0	0	0
Loading (100% excess Li)	mg cm^{-2}	1.726	2.072	1.035	1.035
Density	g cm^{-3}	0.53	0.53	0.53	0.53
Porosity	%	0%	0%	0%	0%
Thickness	μm	3.3	3.9	2.0	2.0
Active Mat. Percentage	%	100%	100%	100%	100%

Areal Capacity	mAh cm^{-2}	6.66	8.00	4.00	4.00
Separator					
Thickness	μm	20	20	20	20
Porosity	%	38%	38%	38%	38%
Density	mg cm^{-2}	0.4	0.4	0.4	0.4
Electrolyte					
Total Volume	cm^3 cm^{-2}	0.0072	0.0111	0.0055	0.0042
Density	g cm^{-3}	1.2	1.11	1.3	1.3
Filling ratio	%	100%	100%	100%	100%
Current Collector					
Thickness of Al	μm	12	12	12	12
Thickness of Cu	μm	6	6	6	6
Specific Energy	Wh kg^{-1}	477	346	312	443
Energy Density	Wh L^{-1}	1102	1023	815	1150

Supplementary References

1 Linstrom, P. J. & Mallard, W. G. NIST Chemistry WebBook, NIST Standard Reference Database Number 69. National Institute of Standards and Technology (2025).

2 Jain, A. et al. Commentary: The Materials Project: A materials genome approach to accelerating materials innovation. *APL Mater.* **1**, 011002 (2013).

3 Liu, S. et al. An inorganic-rich solid electrolyte interphase for advanced lithium-metal batteries in carbonate electrolytes. *Angew. Chem. Int. Ed.* **60**, 3661–3671 (2021).

4 Yu, W. et al. Electrochemical formation of bis(fluorosulfonyl)imide-derived solid-electrolyte interphase at Li-metal potential. *Nat. Chem.* **17**, 246–255 (2025).